High-resolution valence-band XPS spectra of the nonconductors quartz and olivine

V. P. Zakaznova-Herzog,[1,*] H. W. Nesbitt,[1] G. M. Bancroft,[2] J. S. Tse,[3] X. Gao,[4] and W. Skinner[5]
[1]*Department of Earth Sciences, University of Western Ontario, London, Ontario, Canada N6A 5B7*
[2]*Department of Chemistry, University of Western Ontario, London, Ontario, Canada N6A 5B7*
[3]*Department of Physics and Engineering, University of Saskatchewan, Saskatoon, Saskatchewan, Canada S7N 5E2*
[4]*Steacie Institute for Molecular Sciences, National Research Council of Canada, Ottawa, Ontario, Canada K1A 0R5*
[5]*Ian Wark Research Institute, University of South Australia, Adelaide, Australia SA 5095*
(Received 16 June 2005; revised manuscript received 19 September 2005; published 9 November 2005)

High-resolution core-level and valence-band x-ray photoelectron spectra (XPS) of the nonconductor silicates, quartz, and two olivines ($[Mg,Fe]_2SiO_4$, Mg rich and Fe rich) have been obtained with the Kratos magnetic confinement charge compensation system which minimizes differential charge broadening. Observed total linewidths are about 1.3 eV for several of the peaks in these spectra, much narrower than previously obtained. The quartz and olivine valence-band spectra are very different, even though the dominant contributions to both come from molecular orbitals of SiO_4 groups. High-quality calculations of the band structure using pseudopotential density functional theory with generalized gradient approximation (GGA) for quartz yield a theoretical XPS valence-band spectrum in the Gelius approximation that is in excellent agreement with the experimental spectrum. GGA+U (where U is the on-site Coulomb energy) calculations on Mg-rich and Fe-rich olivines yield theoretical XPS spectra in good qualitative agreement with experiment. The valence-band spectral contributions are readily assigned using the calculated partial density of states. For example, the Fe 3d t_{2g} and e_g orbitals in $M1$ and $M2$ sites of the olivine are located at the top of the olivine valence band and are readily resolved in both observed spectra and theoretical calculations. The valence-band spectrum of quartz is about 3 eV more dispersed than the valence bands of the olivines and considerably greater than the 1.4 eV difference calculated previously. The difference in dispersion arises mainly from two effects. The dispersion of the quartz valence band is primarily a response to the nature of metal atoms in the second coordination sphere of the central Si atom of SiO_4 tetrahedra. For example, the Si-O moiety is more negatively charged in olivine than in quartz because of the transfer of electrons from Mg to O-Si. The calculations indicate very small Mg 2s contributions to the forsterite (Mg_2SiO_4) valence band. Hence all Mg 2s electrons effectively reside on O atoms (O 2p orbitals) and the Mg-O bond is ionic. Polymerization (network formation) also contributes to dispersion in that it results in large splittings in the Si 3s and Si 3p partial density of states. Fe 3d electrons of olivines are of both "bonding" and "nonbonding" according to the calculations. In the Mg-rich olivine, the great majority of Fe 3d electrons are nonbonding and give rise to separate Fe 3d t_{2g} and e_g peaks at the top of the valence band. The same no-bonding contributions are observed in Fe-rich olivine, but O 2p contributions near the top of the valence band indicate appreciable Fe-O bonding.

DOI: 10.1103/PhysRevB.72.205113 PACS number(s): 71.20.−b, 79.60.Bm, 71.15.Mb

I. INTRODUCTION

Core-level x-ray photoelectron spectroscopy (XPS) has been used for many years to study the surface reactivity of nonconductor silicate minerals to determine surface elemental compositions and to study the mechanisms of reaction in aqueous solutions.[1–5] Because of the large and inconsistent linewidths resulting from differential charging, core-level chemical shifts generally have not been sufficient to obtain chemical information on Si and other constituent elements of silicates. Valence-band XPS spectra (often using low-energy synchrotron sources) of semiconductor sulfides such as pyrite (FeS_2), for example, combined with theoretical calculations have been very useful to obtain bonding and reactivity information.[6,7] Such valence-band spectra should also be useful to determine the bonding and reactivity of nonconducting silicates.

The very low valence-band cross sections at 1487 eV photon energy (Al $K\alpha$ source) and differential charging problems make it extremely difficult to collect meaningful valence-band x-ray photoelectron spectra (VBXPS) of silicates. Indeed, to the best of our knowledge, the VBXPS have been reported on only two silicate minerals, α-quartz (α-SiO_2) (Refs. 8 and 9) and a Mg-rich olivine ($[Mg,Fe]_2SiO_4$) (Refs. 10 and 11), although VBXPS spectra have been published for Na, Li, and Ca silicate glasses[12,13] and a number of analogous phosphate powders[14] The good-quality spectra of α-quartz have been compared with the spectra of amorphous SiO_2 films on Si (Si substrate used to alleviate charging problems) (Refs. 8 and 15) and with theoretical calculations.[16–19] The early reported VBXPS spectra of the olivine[10,11] were noisy, broad, and featureless, but were used with x-ray emission spectra and theoretical calculations[20,21] to compare the bonding in olivine and quartz in a qualitative manner.

Because of the very long counting times required to collect high-resolution valence bands of nonconductors (typically several hours), the stability of the charge compensation system of most XPS instruments is severely tested. The large XPS linewidths from bulk nonconductors has been attributed

to the differential charging of these surfaces,[22] and electron flood guns have been employed to try to minimize this broadening.[23] A recent development now makes it possible to collect VBXPS spectra of nonconductor silicates (and all nonconductors) with considerably greater resolution than heretofore possible. The new Kratos XPS instruments use a novel magnetic confinement charge compensation system[24] which effectively eliminates differential charging in nonconductors and yields narrower and consistent core-level linewidths on nonconductor minerals, including a Mg-rich olivine.[25] Indeed, the comparison of core-level XPS spectra of analogous semiconductor and nonconductor minerals[25] indicates that the nonconductor linewidths can be as narrow as for the analogous semiconductor (0.5 eV at room temperature using a monochromatized Al $K\alpha$ source).

Recent computational developments permit high-quality band-structural calculations for solids, including quartz and olivines.[26–28] With this development, it is possible to assign VBXPS contributions to spectra where available. In this regard, we report high-resolution core and valence-band XPS of α-quartz (SiO_2) and two olivines, one Mg rich and the other Fe rich [members of the forsterite (Mg_2SiO_4)-fayalite (Fe_2SiO_4) solid-solution series]. The collected spectra are compared and contrasted with our density-functional-theoretical calculations. The narrow linewidths ($\sim$1 eV) observed in the olivine valence bands and the agreement with calculations make it possible for the first time to unambiguously assign these spectra. These valence-band spectra are very sensitive chemically, and it is expected that similar experimental and theoretical studies will be very useful for understanding the physical and chemical properties of a large number of silicate minerals and glasses, as well as nanocrystalline silica samples used for optoelectronic purposes.

II. EXPERIMENT

Gem-quality minerals were obtained for quartz and the two olivines from the mineral collections at the University of Western Ontario and the South Australian Museum. The Mg-rich olivine ($[Mg_{0.87}Fe_{0.13}]_2SiO_4$) was taken from a sample used for a previous core-level XPS study.[25] The Fe-rich olivine was characterized both structurally (XRD spectra) and compositionally by a JEOL JXA-8600 superprobe electron microprobe, with the following result: $(Mg_{0.14}Fe_{0.86})_2SiO_4$. All samples were cleaved *in situ* in the vacuum of the introduction chamber (low-10^{-8} torr range) system and immediately transferred to the analytical chamber where pressures were in the low-10^{-9} torr range. A Kratos axis ultra x-ray photoelectron spectrometer (with magnetic confinement charge compensation system) at Surface Science Western (SSW) was used to collect the room-temperature XPS spectra using Al $K\alpha$ radiation at 1487 eV and a 300-μm spot size for all analyses. A 10 eV pass energy was used to collect all core levels (Si 2p, Mg 2p, and O 1s), and 20 eV pass energy was employed to collect all valence-band spectra. The instrumental resolution at 10 eV pass energy is about 0.35 eV.[24,25] The low C 1s signal indicated minimal C contamination (maximum of a few atomic percent C). The charge compensation system was tested for effectiveness over a large range of settings with only small changes in linewidths. Optimal settings yielded Si $2p_{3/2}$ linewidths of 1.0–1.1 eV (1.2–1.3 eV for O 1s), and these were highly reproducible over months of testing. The takeoff angle was usually 90°, but spectra were also taken at a 60° takeoff angle. All binding energies were referenced to the adventitious C 1s peak at 285.0 eV.

Core-level spectra were fit with a 50%-Gaussian–50%-Lorentzian function for doublets and 70%-Gaussian–30%-Lorentzian function for the total spectral envelope. Spin-orbit components were constrained to have the same linewidths. The spin-orbit splitting was fixed to atomic values, and the $p_{1/2}$ peak was constrained to half the intensity of the $p_{3/2}$ peak. The spin-orbit splitting parameters used are 0.617 eV for the Si 2p (Ref. 29) and 0.28 eV for Mg 2p. (Ref. 30). Because of the constraints on the $p_{1/2}$ position, linewidth, and intensity, just the $p_{3/2}$ position and linewidth were iterated to minimize the root-mean-square deviations for a given spectrum. The Si and Mg orbital splittings were unresolved in these spectra, so that peak widths [full width at half maximum (FWHM)] were evaluated by the best visual fit of the low-energy side of the Si 2p and Mg 2p peaks. All spectra were corrected for the background using the Shirley approach.[31]

III. THEORY

Electronic structural calculations within the pseudopotential density function theory (DFT) with generalized gradient approximation[32] (GGA) were performed with the program SIESTA.[33] In these calculations the effect of core electrons is replaced by a Troullier-Martin-type pseudopotential.[34] For the valence orbitals, Sankey[35] double-ζ basis sets augmented with a set of d-polarization functions were used for Si, O, and Mg, and for Fe, a double-ζ basis for Fe 3d and 4s augmented with a 4p polarization function was employed. Calculations were performed at the experimental geometries[36] of α-quartz (SiO_2), Mg_2SiO_4, and Fe_2SiO_4. The calculation on an Mg-rich (Fe-doped) olivine of $(Mg_{0.875}Fe_{0.125})_2SiO_4$ composition used the same structure as Mg_2SiO_4 with one Mg out of eight replaced by Fe in the $M2$ site. The DFT was found to give good electronic band structure for quartz and forsterite (Mg_2SiO_4). For $(Mg_{0.875}Fe_{0.125})_2SiO_4$, spin-polarized GGA calculations assuming the Fe atom is in the high-spin state predicted an insulator ground state with a small band gap. To investigate possible effects of orbital localization and correlations, calculations using the GGA+U method[37] as implemented in the electronic code VASP8 (Ref. 38) were also performed. For Fe_2SiO_4, the localized density approximation even with the GGA predicted, incorrectly, a metallic ground state. In this case, to account for the electron correlation effect, GGA+U calculations were performed employing the parameters used in a recent calculation on Fe_2SiO_4.[39]

Following the Gelius model,[40] the valence-level x-ray photoelectron spectra were calculated from the theoretical projected density of states of individual atoms weighted by the corresponding theoretical atomic cross sections.[41] All peaks were broadened with a Gaussian experimental width of

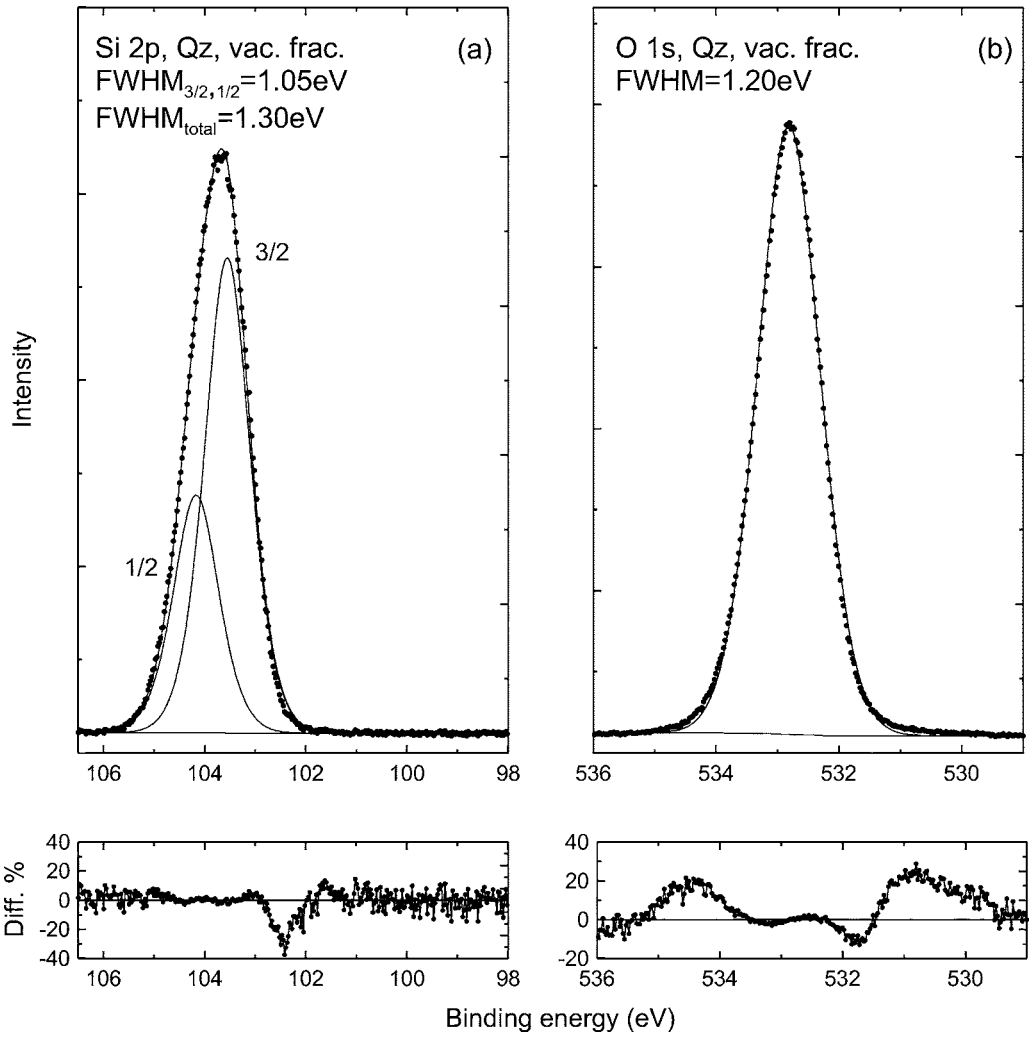

FIG. 1. Core-level XPS spectra of quartz: (a) Si 2*p* and (b) O 1*s*. Residuals from the least-squares fit are shown below the spectra.

0.37 eV, a value similar to the measured instrumental resolution of 0.35 eV.

IV. RESULTS AND DISCUSSION

A. Core-level XPS spectra

Core-level XPS spectra for quartz and the Mg-rich olivine are shown in Figs. 1 and 2 and core-level binding energies and linewidths for individual spectra. Individual results are given in Table I to illustrate the excellent reproducibility of spectra taken on different parts of the same samples and on different days. The fits to the spectra in Figs. 1 and 2 are generally satisfactory, but the O 1*s* fits show considerable deviations from the experiment, especially at high binding energy, and probably are due to a small amount of OH^- on the surface. The total Si 2*p* linewidth for the Mg-rich olivine is 1.26 eV (the average of four independent spectra being 1.29 eV, Table I) and is similar to, but slightly narrower than, that previously reported (1.36 eV) from a *polished* sample using the same instrument.[25] The linewidths of the spin-orbit components (Si and Mg $2p_{3/2}$ and $2p_{1/2}$) for this sample are about 1.0 eV [Figs. 2(a) and 2(c)] whereas the Si $2p_{3/2,1/2}$ linewidths for quartz [Fig. 1(a)] are slightly larger at 1.1 eV. Because of the problem of differential charge broadening, there have been very few linewidths for any silicates reported in the literature but most spectra taken on modern monochromatic XPS instruments give linewidths greater than 2 eV (for example, Si 2*s* and O 1*s* spectra of an Fe-rich olivine[4] and Si 2*p*, Al 2*p*, and O 1*s* spectra of feldspars[42]). The Si 2*p* and O 1*s* binding energies for the quartz and Mg-rich olivine spectra are in good agreement with recently reported values[4,43] once a correction to a common reference energy is made (Au 4*f* at 84.0 eV). As noted previously,[4,43] both O 1*s* and Si 2*p* binding energies (BE's) for Mg-rich olivine are about 1.8 eV lower than for quartz, which is consistent with the O and Si in olivine being considerably more negatively charged than the O and Si in quartz.

The Si 2*p*, Mg 2*p*, and O 1*s* linewidths for quartz and olivines in Table I are similar. The total Si 2*p* envelop linewidth on quartz (1.38 eV in Table I) is also similar to, but less than, that reported previously (1.42 eV) from a high-resolution synchrotron XPS study of a thin noncharging amorphous SiO_2 layer on Si.[44] This conformity is testament to the absence of differential charge broadening in our conventional spectra (Figs. 1 and 2). As previously argued,[25] the

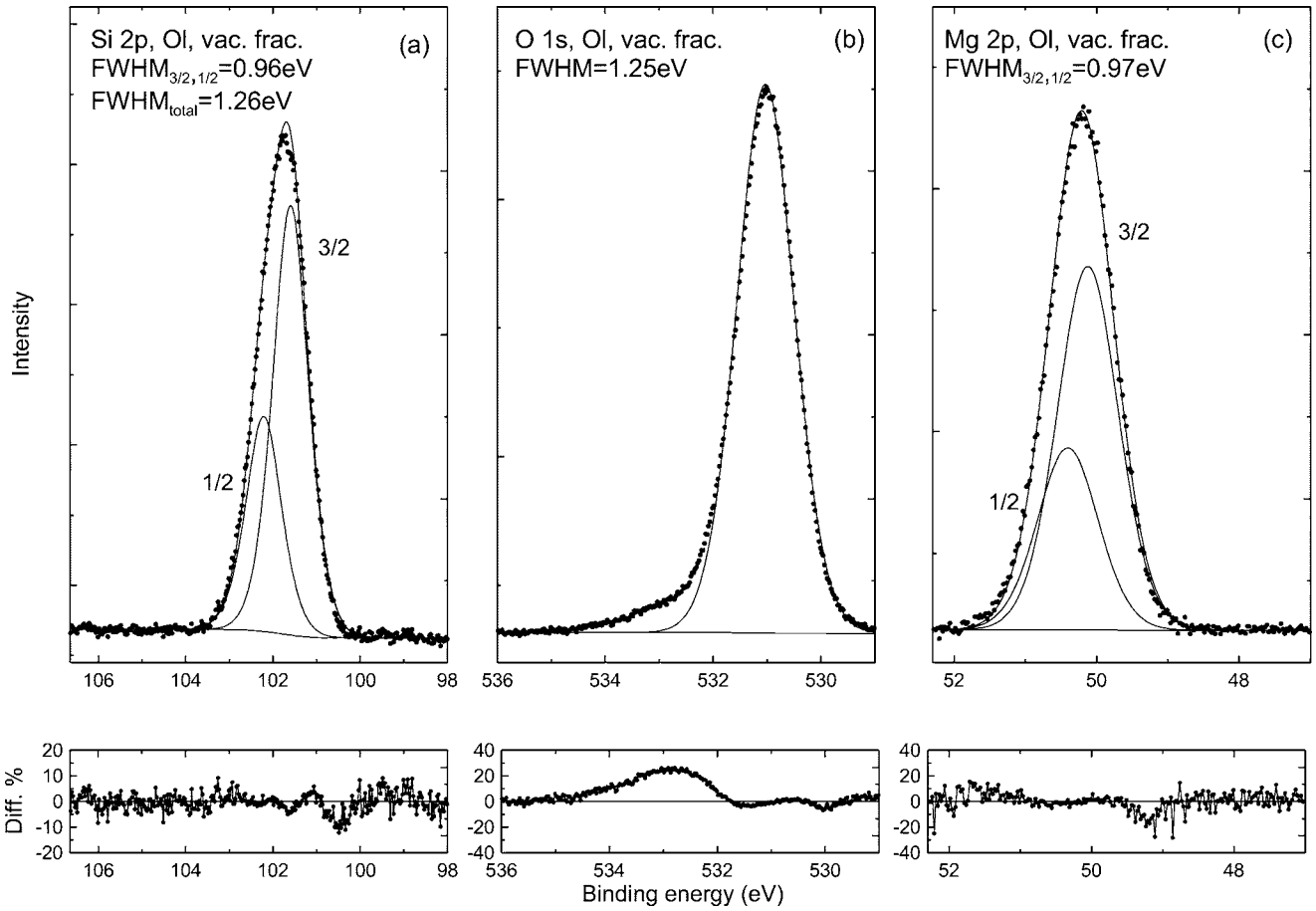

FIG. 2. Core-level spectra of Mg-rich olivine $(Mg_{0.87}Fe_{0.13})_2SiO_4$: (a) Si 2*p*, (b) O 1*s*, and (c) Mg 2*p*.

Si 2*p* linewidths are dominated by the final-state vibrational splitting from the totally symmetric Si-O vibrational mode in the two minerals. Indeed, the slightly narrower linewidths observed in this study are better fit using the Si-O vibrational pattern in the analog molecule $Si(OCH_3)_4$ than the spectrum reported in the previous paper [see Fig. 3(b) in Ref. 25]. The similar Si 2*p*, Mg 2*p*, and O 1*s* linewidths in our three silicates strongly suggest that the linewidths of Mg 2*p* and O 1*s* spectra are also the result of a vibrational envelope. These linewidths must be very close to the minimum room-temperature linewidths for our instrumental linewidth of about 0.35 eV.[25] For Si 2*p* XPS spectra of Si metal, there is no vibrational broadening or differential charging and Si $2p_{3/2}$ linewidths of <0.4 eV are obtained.[44] The final-state vibrational broadening is not temperature dependent, but phonon broadening of each vibrational peak is temperature

TABLE I. Binding energies[a] and total linewidths (eV) for XPS spectra.

Mineral	Si 2*p*	FWHM	O 1*s*	FWHM	O 2*s*	FWHM	Mg 2*p*	FWHM
Quartz	103.7	1.43	532.8	1.22	25.7	3.28		
Quartz	103.5	1.42	532.6	1.28	25.5	3.15		
Quartz	103.7	1.30	533.0	1.20	25.7	3.03		
Qz average	103.6	1.38	532.8	1.23	25.6	3.15		
Mg-rich olivine	101.9	1.33	531.2	1.28			50.4	
Mg-rich olivine	101.6	1.27	530.8	1.26	23.0	2.94	50.0	1.10
Mg-rich olivine	101.8	1.26	531.0	1.25	23.2	2.97	50.2	1.05
Mg-rich olivine	101.6	1.30	530.8	1.26	23.0	2.99	50.0	1.05
Mg-rich olivine average	101.7	1.29	531.0	1.26	23.1	2.97	50.2	1.07
Fe-rich olivine	101.9	1.30	531.2	1.26				

[a]Calibrated relative to C 1*s* at 285.0 eV.

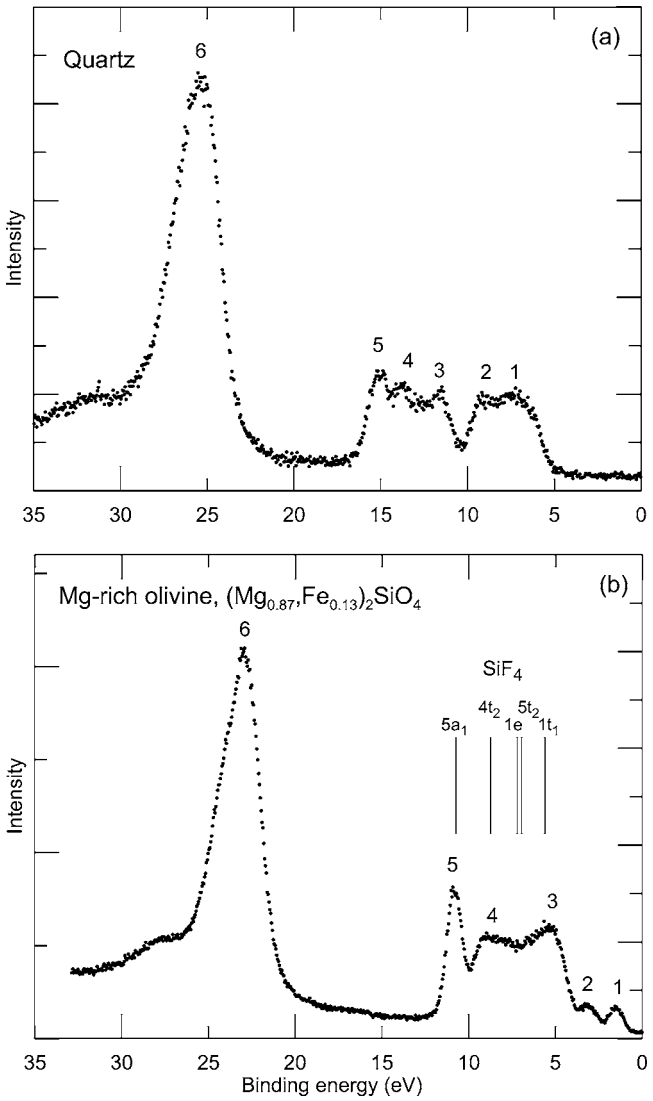

FIG. 3. The "O 2*s*" and valence-band XPS spectra (VBXPS) of (a) quartz and (b) Mg-rich olivine.

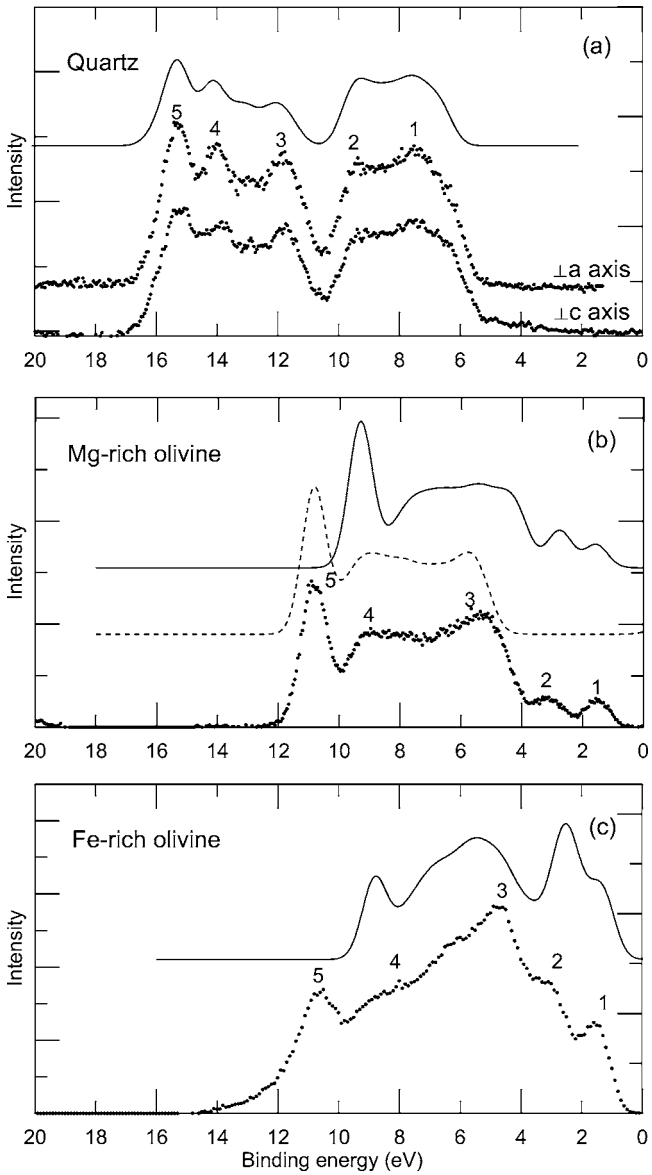

FIG. 4. The VBXPS spectra (dotted lines) of (a) quartz at two different orientations, (b) Mg-rich olivine, and (c) Fe-rich olivine. The calculated XPS spectra (solid and dashed lines) for the quartz and two olivines of similar composition to the two natural olivines are given above the experimental spectra. The intensity of each state was corrected for cross section and each band broadened by 0.37 eV to match the instrumental resolution. The calculated quartz spectrum was aligned to the experimental spectrum of quartz, and the calculated olivine spectra (solid lines) were aligned to the experimental energies of peak 1 (the Fe 3*d* band). The calculated forsterite spectrum (dashed line) was aligned to the experimental energies of peak 5 (the Fe 3*d* band).

dependent and adds about 0.1 eV at room temperature to the width of each of the ten vibrational peaks,[45] but less than 0.05 eV to the overall composite linewidths.

B. Valence-band spectra and qualitative interpretation

The valence-band spectra of quartz and Mg-rich olivine, including the O 2*s* peaks near 25 eV, are shown in Fig. 3. The quartz spectrum is similar to those published previously,[8,9] although our resolution is somewhat better, as apparent from the better resolution of peaks 1 and 2 and the deeper minimum between peaks 2 and 3. Our quartz spectrum is shifted about 5 eV to higher energy (calibrated with C 1*s* at 285.0 eV) compared with previously reported spectral energies; previous studies set the lowest-energy signal (the "top" of the valence band) at 0 eV. The shift is necessary to plot the quartz and olivine spectra on the same scale. Furthermore, the 5 eV shift is consistent with our 0 eV being a fictitious "Fermi" level at the midpoint of the ~10 eV band gap in quartz.[16,17,19] The outer valence-band spectra of quartz and a Mg-rich and a Fe-rich olivine are shown in Fig. 4, along with calculated spectra that will be discussed later. Quartz spectra were collected normal to two crystallographic axes [Fig. 4(a)] and indicate a rather small amount of band dispersion. This, however, is not surprising in that all surfaces analyzed were of a conchoidal nature and many crystallographic orientations will contribute to both spectra.

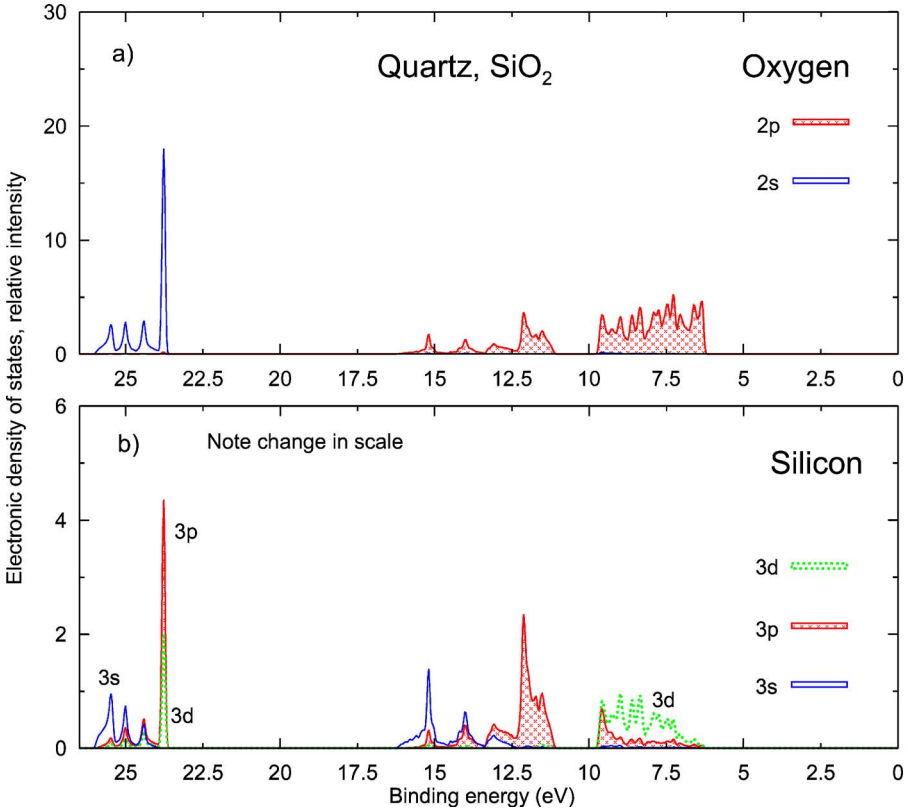

FIG. 5. (Color online) Partial density of states for the valence band of quartz: (a) oxygen partial density of states and (b) silicon partial density of states. Note that the Si intensities have been exaggerated by 5 times relative to the O intensities.

Spectra of the Mg-rich olivine [Figs. 3(b) and 4(b)] do not resemble the low-quality spectra published previously.[10,11] Perhaps most surprising are the narrow (~1 eV) linewidths for peaks 1, 2, and 5 [Fig. 4(b)]. The spectrum of Fig. 4(b) was collected at a 60° takeoff angle, whereas that of Fig. 3(b) was collected at 90°, suggesting a small dispersion of the bands in k space (surfaces also conchoidal). As for quartz, all olivine valence-band spectra were calibrated with the C 1s peak at 285.0 eV. Our calibration method places the Fe 3d bands close to the top of the valence band as previously calculated.[26,39] The calibration is also consistent with an experimental and theoretical energy gap (top of valence band to the bottom of the conduction band) in Mg_2SiO_4 of about 9 eV (Ref. 27) with the "Fermi" level being at the middle of the band gap. The narrow linewidths, from individual spectra representing hours of collection, attest to the great stability of the charge compensation system.

The quartz VB spectrum [Fig. 3(b)] has been assigned qualitatively, based on molecular orbital (MO) considerations for a tetrahedral SiO_4 unit.[8,9] This spectrum is qualitatively the same as spectra of the analogous tetrahedral $Si(OCH_3)_4$ and SiF_4 gas-phase molecules[29,46] [see shifted gas-phase SiF_4 energies in Fig. 3(b)]. Peaks 1 and 2 are loosely associated with the nonbonding O 2p 1e, 5t_2, and 1t_1 orbitals. Peaks 3 and 4 are associated with the 5a_1 and 4t_2 orbitals, which are σ-bonding orbitals, both resulting from O 2p–Si 3p mixing. Peak 5, also observed in the previous study,[8,9] had been assigned to the K 3p line from a potassium impurity,[8,9] but this assignment is incorrect because there is very little K in most quartz samples; our sample contains a sub-ppm level of K (undetectable by XPS at this concentration), yet the peak-5 signal is strong. Peak 6 is associated with 3t_2 and 4a_1 molecular orbitals derived from mixing of O 2s with a small amount of Si 3p and Si 3s.

Qualitatively, the olivine VB spectra can be assigned using MO considerations. The two olivine spectra display five peaks with each at a similar energy; apparently, these peaks are characteristic of the olivine structure. Peaks 1 and 2 can be attributed to excitation of photoelectrons from the Fe 3d e_g and t_{2g} orbitals, respectively, as expected from previous calculations where Fe 3d orbitals are located at a very low BE.[28,39] The splitting of peaks 1 and 2 is about 1.4 eV in the XPS spectra, which compares favorably with observed crystal-field splitting of about 1.2 and 1.0 eV for the $M1$ and $M2$ sites in an olivine.[47,48] The intensity of peaks 1 and 2 increases considerably from Fig. 4(a) and 4(b), an observation consistent with the increased abundance of Fe in the Fe-rich olivine.

As predicted by Tossell,[20,21] the valence band of olivine is energetically compressed relative to that of quartz. The dispersion is about 10 eV for quartz and about 7 eV for olivine (Fig. 3) if the Fe 3d peaks 1 and 2 are ignored, and the difference requires explanation.

C. Band structure, calculations, and assignments

State-of-the-art valence-band calculations were conducted to understand better the nature of the valence-band contributions and their dispersion. The partial densities of states for the quartz, forsterite (Mg_2SiO_4), the Mg-rich (Fe-doped) olivine, and fayalite (Fe_2SiO_4) are given in Figs. 5–8, respectively. The energies shown were calibrated to match the experimental spectrum of quartz and the lowest-energy Fe 3d band of olivines. Although these partial density of states

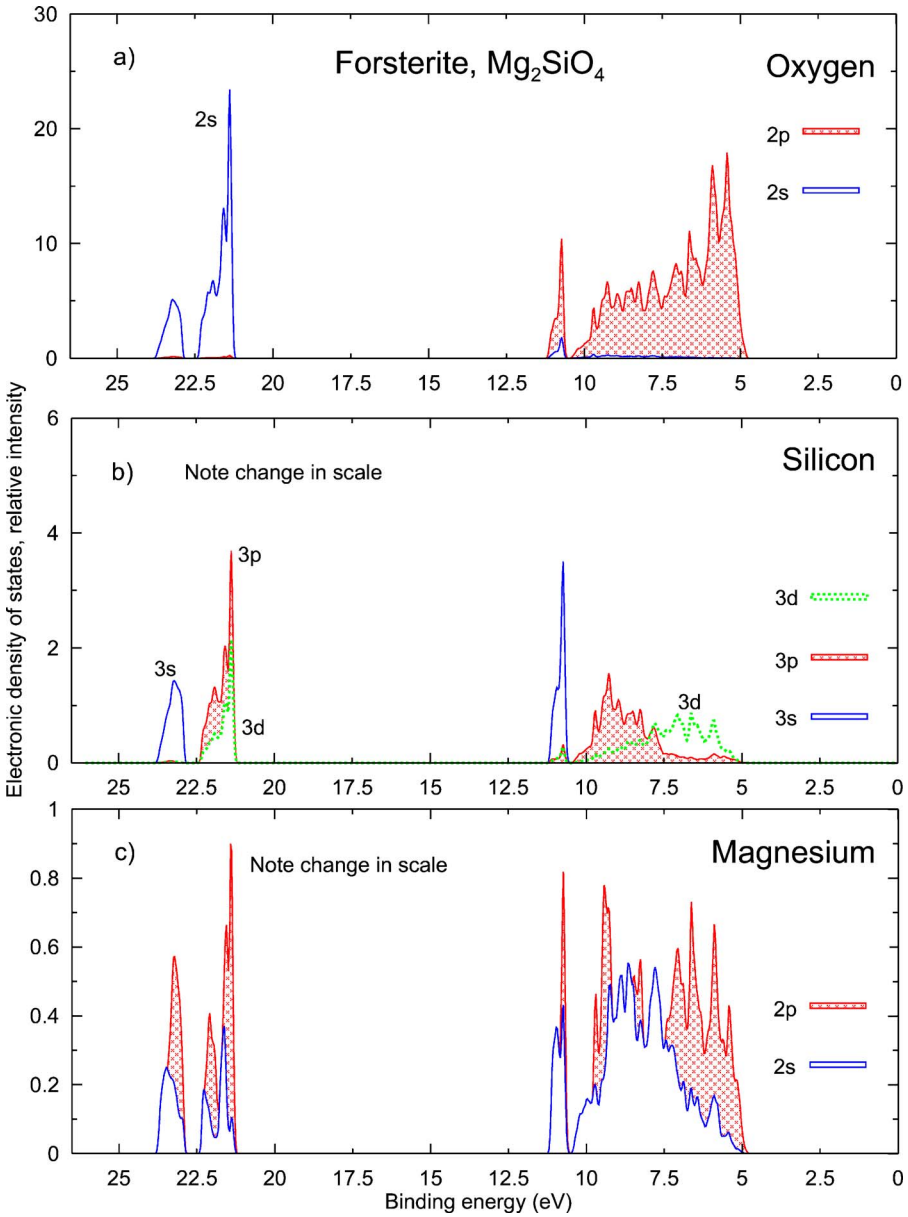

FIG. 6. (Color online) Partial density of states for the valence-band region forsterite: (a) oxygen partial density of states, (b) silicon partial density of states, and (c) magnesium partial density of states. Note the exaggeration of the Si (5 times) and Mg (30 times) intensities relative to O.

compare favorably with previous calculations on quartz and the two olivine end members,[17,19,26–28] these can be compared with previous calculations in a gross sense only because previous figures were very small and the partial densities of states were given only for the Fe contributions to Fe_2SiO_4.[28,39] However, previous calculations do show the same two-peak Fe 3*d* structure at the top of the valence band.[39]

There has been no previous attempt to quantitatively compare calculations with the spectra of the quartz valence band. Indeed, the peak at about 15 eV (Fig. 4) has not been assigned. The outer valence spectral and calculated dispersion of the quartz valence band match exactly, and every feature in the spectrum (with a broadening function of only 0.37 eV) is reproduced, including all five major peaks, the shoulder on the low-BE side of peak 1, and the small peak between peaks 3 and 4. Even the relative intensities and the magnitude of the minimum between peaks 2 and 3 are well reproduced by the calculation. However, the O 2*s* outer valence regions are not well reproduced by the calculations. For example, the experimental O 2*s* peak has a BE of about 25 eV [Fig. 3(a)], whereas the theoretical BE [Fig. 5(a)] is about 23.5 eV. Moreover, there are very significant shoulders at high BE for these spectra [>30 eV for quartz, Fig. 3(b)], which are not reproduced by the calculations. These discrepancies are expected[49] because of the complete breakdown of the one-electron approximation in the inner valence region, giving many peaks arising from states that are admixtures of single-hole states and multihole states.

The agreement between theory and experiment is less satisfactory for the olivine outer valence-band spectra [Figs. 4(b) and 4(c)], although there is good qualitative agreement. The GGA+U calculations on both the Mg-rich (Fe-doped) olivine and fayalite reproduce the observed decrease in dispersion of the olivine bands relative to that of quartz and demonstrate that this decreased dispersion is constant across the olivine solid-solution series. The observed five peaks are reproduced by the calculation, with intensities and linewidths

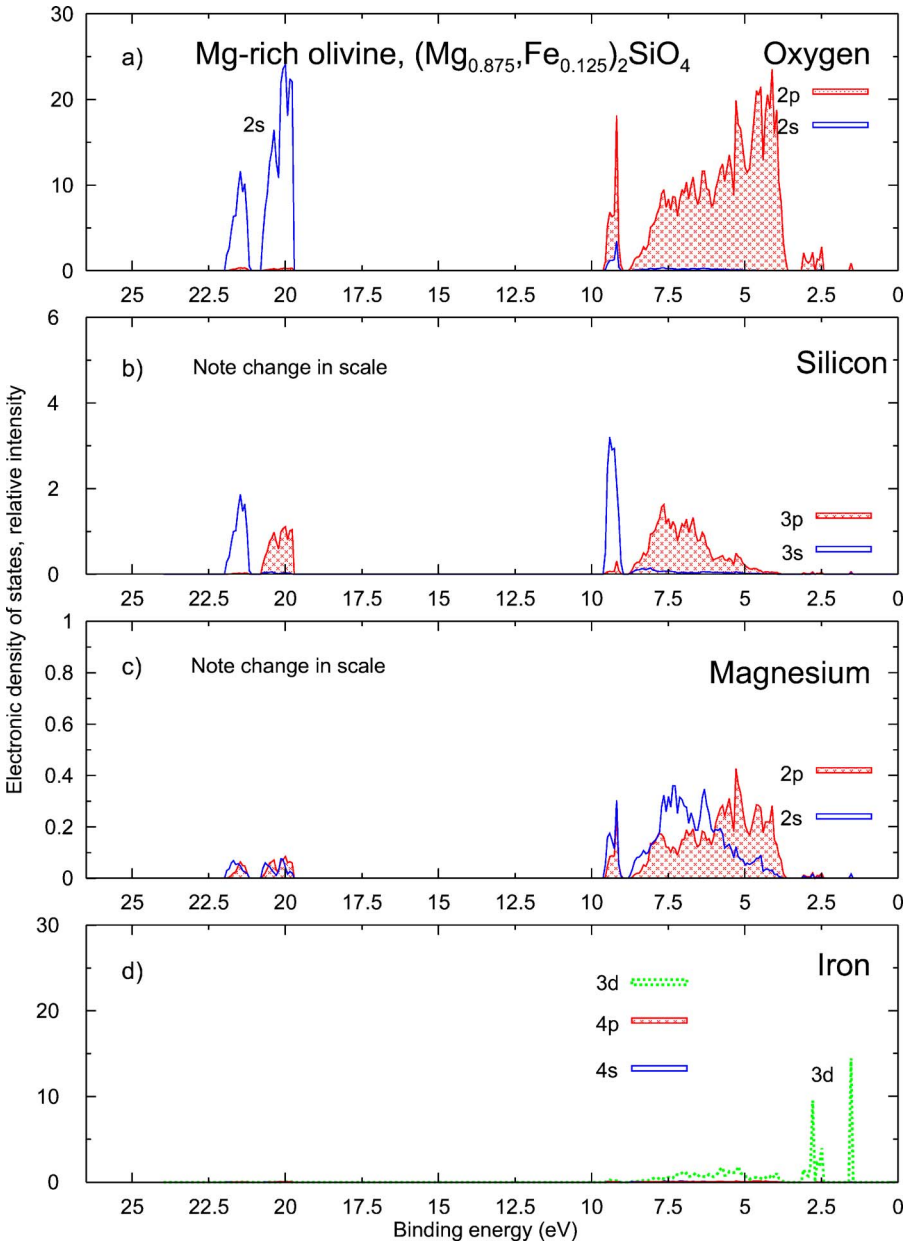

FIG. 7. (Color online) Partial density of states for the valence band of Mg-rich olivine $(Mg_{0.87}Fe_{0.13})_2SiO_4$ from the GGA+U calculation: (a) oxygen partial density of states, (b) silicon partial density of states, (c) magnesium partial density of states, and (d) iron partial density of states. Note the exaggeration of the Si and Mg intensities relative to O intensities.

similar to those observed (bands broadened to 0.37 eV and cross sections considered). The calculations underestimate the overall dispersion, and the Fe 3*d* peaks (peaks 1 and 2) are somewhat too close in energy to peak 3 (peak 3 arises mainly from O 2*p* orbitals), as apparent in Fig. 9. The Fe-O hybridization may be overestimated in our calculations on the two Fe-containing olivines.

Unlike the spectra of the Fe oxides,[50–52] the olivine spectra can be interpreted largely on the basis of initial states. Nevertheless, the calculations for fayalite underestimate appreciably the intensities between 4 and 6 eV relative to the Fe 3*d* t_{2g}-e_g intensities at the top of the valence band so that there may be some final-state contributions to the deeper valence band as for Fe oxides.[50–52] Alternatively, the Fe 3*d* atomic cross section employed in the Gelius-model calculation may be somewhat too large.

The partial densities of states shown in Figs. 5–9 now are discussed. Peaks 1 and 2 in quartz [Fig. 4(a)] are mostly due to O 2*p* orbitals, with small contributions from Si 3*d* and Si 3*p* orbitals [note that the intensity scale of the Si partial density of states in Fig. 5(b) is expanded fivefold relative to the O 2*p* intensities in Fig. 5(a)]. Peak 3 is mainly due to Si 3*p* and O 2*p* orbitals, with peaks 4 and 5 arising mainly from Si 3*s* and O 2*p* orbitals, with some Si 3*p* contribution. Interestingly, the large Si 3*s* contribution is spread over about 2 eV and contributes to the large dispersion of the quartz valence band. In particular, this splitting gives rise to the previously unassigned peak 5 in Fig. 4(a).

The dispersion of the Si 3*p* and O 2*p* components of the olivine and quartz valence-band spectra is considerably larger than that predicted by Tossell.[20,21] He obtained a 6.4 eV bandwidth for olivine and a 7.8 eV bandwidth for quartz, compared with experimental widths of about 7 eV (olivine) and 11 eV (quartz). Nevertheless, his results are qualitatively in accordance with these spectra and his explanation for the different dispersion applies in a qualitative

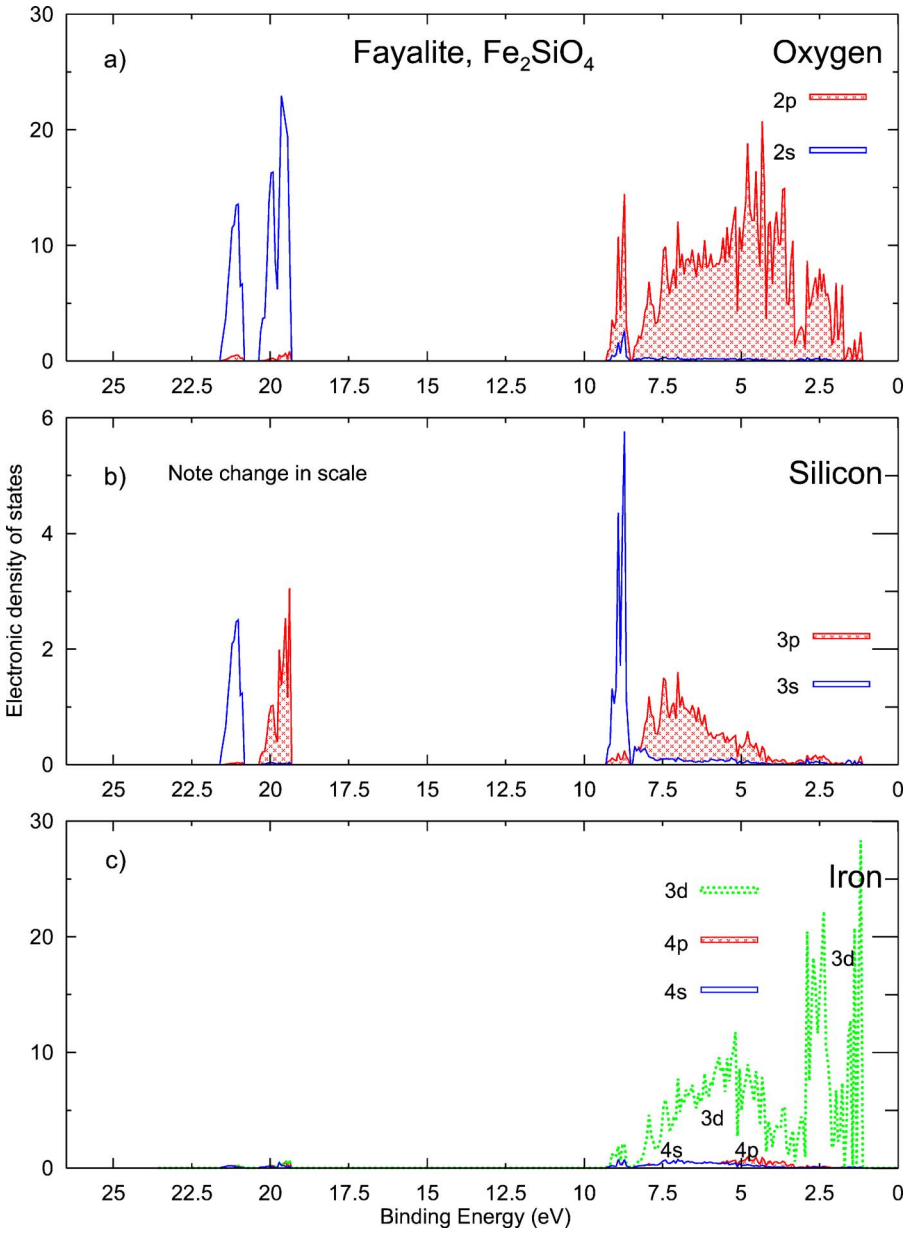

FIG. 8. (Color online) Partial density of states for the valence band of fayalite from the GGA $+U$ calculation: (a) oxygen partial density of states, (b) silicon partial density of states, and (c) iron partial density of states. Note the exaggeration of the Si (5 times) intensity relative to O.

sense. The condensed nature of the olivine valence band was attributed to weaker Si-O bonding in olivine, with destabilization of the $5a_1$ and $4t_2$ orbitals of the SiO_4^{4-} unit in olivine relative to quartz. The weaker bonding cannot be ascribed to the Si-O bond length[20,21] in quartz (1.61 Å) and olivine (1.63 Å); calculations based on these two Si-O bond lengths changed the dispersion of these valence-band peaks by only 0.1 eV.[20] This led Tossell to suggest that the difference in dispersion was due either to the nature of the next-nearest-neighbor cations in quartz and olivine (Si and Mg, respectively) or to polymerization (three-dimensional network formation) in quartz. Inspection of the valence band of the gas phase molecule $Si(OCH_4)_4$ (Ref. 29) makes clear that the major cause is the nature of the cation in the second coordination, rather than polymerization; $Si(OCH_4)_4$ is a discrete molecule in the gas phase, yet its valence band is dispersed over about 9 eV, which is similar to that of quartz. Apparently, as the electronegativity of the O bonded to Si increases from quartz to olivine due to the transfer of electrons from Mg to O (as indicated by the large decrease in O 1*s* BE from quartz to olivine of 1.8 eV), the dispersion of the VB decreases—just as it decreases from $SiCl_4$ (6 eV) (Ref. 53) to SiF_4 (5 eV) (Ref. 46). Similarly, the O-C covalent bond in $Si(OCH_3)_4$ decreases the charge on the O, leading to better O-Si covalent overlap and greater dispersion of the valence band; the electronegativity of Mg or C bonded to O of the Si-O moiety greatly affects dispersion of the valence bands, but does not affect appreciably Si-O bond lengths or bond angles.

Nevertheless and as already mentioned, polymerization contributes to dispersion through increased splitting of (primarily) Si 3*s* contributions. Many of the MO's in ethylene are split in polyethylene (particularly the C 2*s*–based MO's in polyethylene), leading to broadening and an increase in dispersion in polyethylene[54,55] relative to ethylene. As already explained, the splitting of the Si 3*s* contributions is due

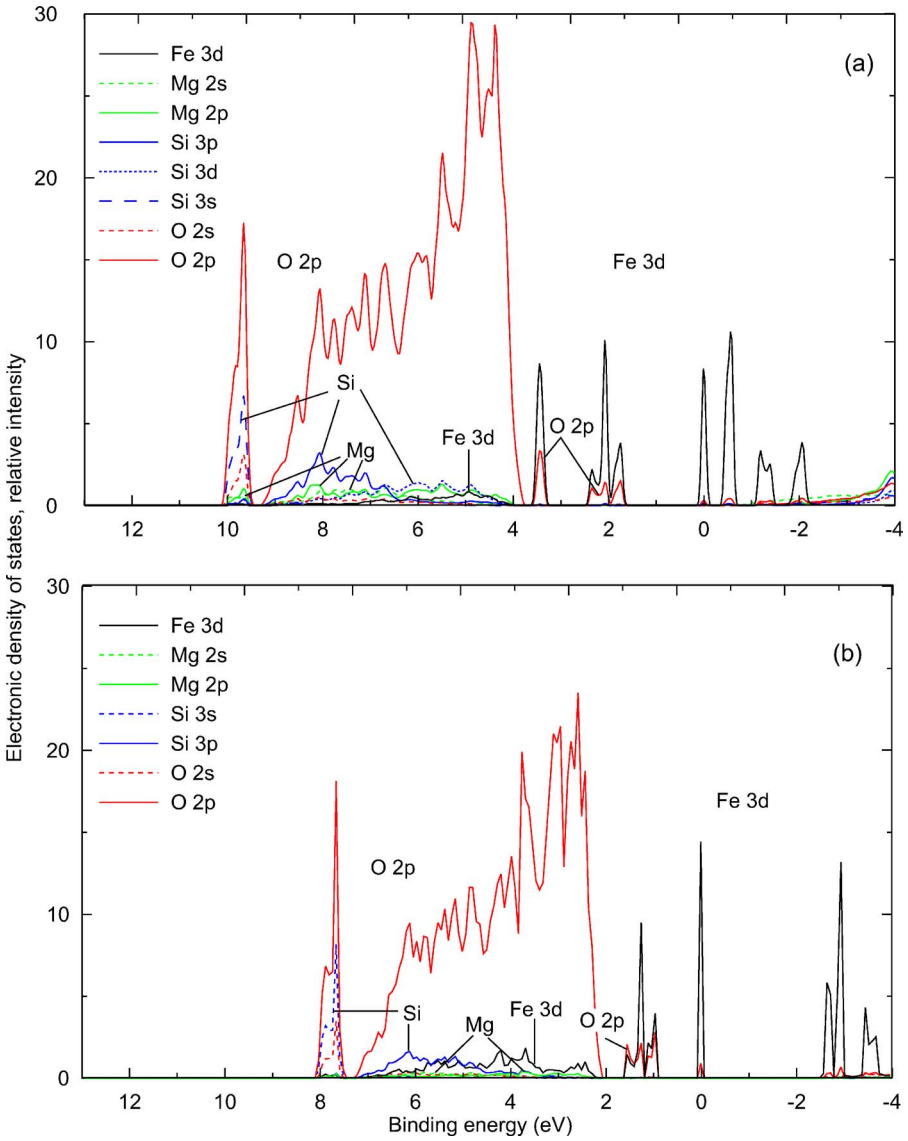

FIG. 9. (Color online) A comparison of the partial density of states of the Mg-rich olivine from (a) GGA calculation and (b) GGA+U calculation.

to polymerization and gives rise to peaks 4 and 5 of quartz [Fig. 4(a)]. The broad peak 6 in Fig. 3(a) also arises from splitting of the Si 3*s* and Si 3*p* orbitals in response to polymerization.

The VB of the Mg-rich olivine [Fig. 4(b)] can be assigned using the partial density of states of forsterite (pure Mg_2SiO_4) in Fig. 6. Peaks 3 and 4 arise almost solely from the O 2*p* contribution [Fig. 6(a)] with much smaller Si 3*p*, Si 3*d*, Mg 2*p*, and Mg 2*s* contributions [Figs. 6(b) and 6(c); note the large exaggeration of scales relative to the O 2*p* intensity]. The narrow peak 5 arises mostly from Si 3*s* and O 2*p* orbital contributions. Again, peak 6 in Fig. 3(b) arises mainly from O 2*s* mixed with some Si 3*p* and 3*s* character. The very small Mg 2*p* and Mg 2*s* contributions confirm that the Mg-O bonding in olivine is highly ionic, as evidenced by the lack of Mg character in the valence bands of our, and previous, calculations.[20,21,26] The much larger O 2*p* contributions in forsterite [Fig. 6(a)] compared to quartz [Fig. 5(a)] are consistent with the almost complete transfer of electrons from Mg 2*s* to O 2*p* in forsterite.

It is tempting, but risky, to comment on the relative instability of Fe-rich olivines based on the two olivine spectra. Partially because of the low BE of the Fe 3*d* density of states, the average outer valence-band binding energy for fayalite is less than that for forsterite (Figs. 6 and 7). Also, the calculated intensity-weighted average binding energy of the Mg-rich olivine is somewhat greater than that for the Fe-rich olivine spectra [7.4 and 6.4 eV, respectively, from Figs. 4(b) and 4(c)]. An implication is that average bond strengths are somewhat weaker in Fe-rich olivine than in Mg-rich olivine. In addition, the O 2*p* contributions at the Fe 3*d* t_{2g} and e_g energies in the fayalite calculation (Fig. 8) indicate appreciable Fe-O bonding at unusually low binding energies (1–3 eV), which again is likely to contribute to weak bond strengths in Fe-rich olivine; the observations may provide a partial explanation for the highly restricted stability of Fe-rich olivine in natural settings.

As apparent from the GGA+U calculations of Figs. 7 and 8, inclusion of Fe in the Mg-rich (Fe-doped) olivine has a minor effect on the dispersion of the Si 3*p* and O 2*p* partial density of states [Figs. 4(b) and 8]. The calculated spectrum of Fe-doped olivine [Fig. 4(b)] is somewhat more condensed than either the experimental result [Fig. 4(b)] or the calculated result for forsterite [Fig. 4(b)]. Calculations incorporat-

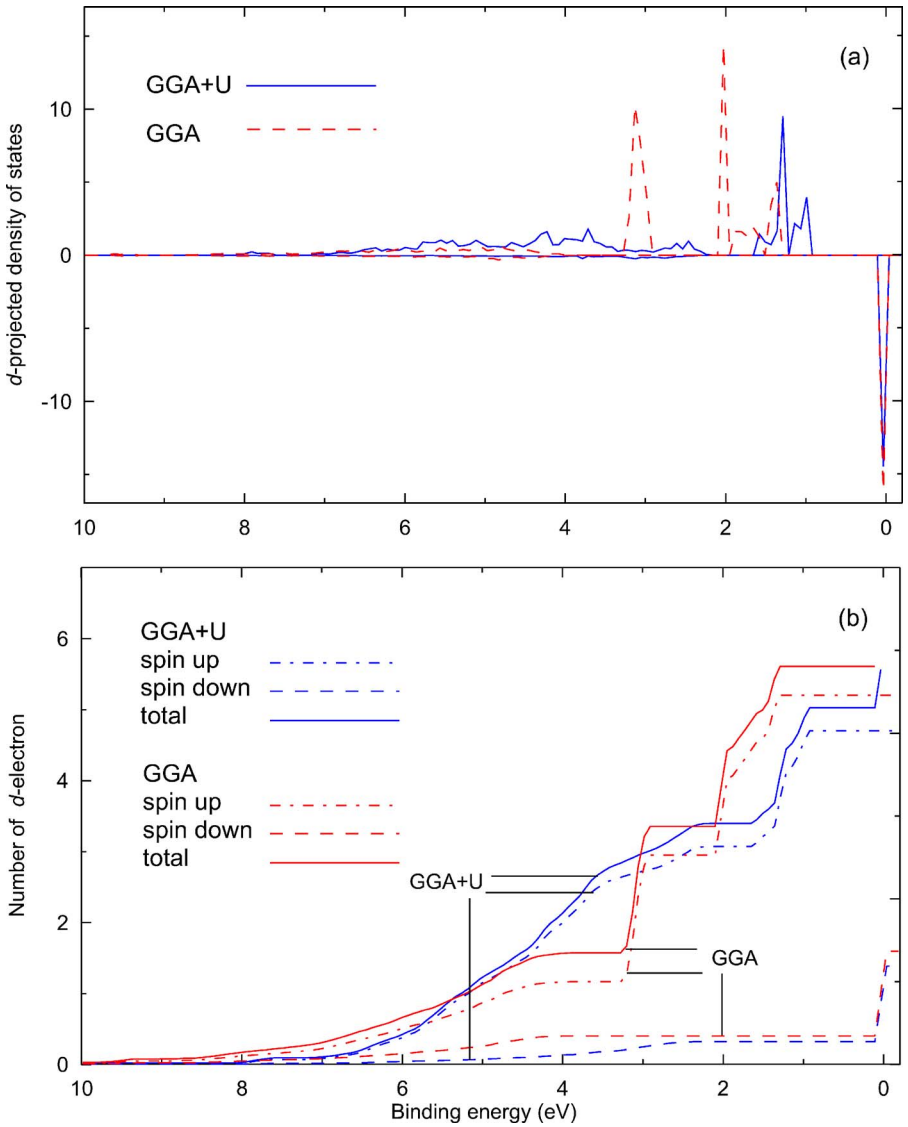

FIG. 10. (Color online) The Fe 3*d* density of states from the GGA and GGA+*U* calculations: (a) the Fe 3*d* density of states as a function of spin state for both calculations and (b) the number of summed Fe 3*d* electrons for both calculations.

ing Fe underestimate somewhat the dispersion of the Fe-bearing olivine spectra, as is apparent by comparison with the dispersion calculated for forsterite Mg_2SiO_4 [Fig. 4(b)]; the latter calculation (with no Fe included) accurately reproduces the dispersion of the Si 3*p* and O 2*p* contributions to the Mg-rich olivine experimental spectrum [Fig. 4(b)]. The theoretical treatment of Fe in these silicates apparently requires additional consideration if Fe-bearing silicate valence bands are to be accurately simulated.

To complete the discussion, it is appropriate to comment on differences between GGA and GGA+*U* calculations for the Mg-rich olivine (Figs. 9 and 10). Following the conventional theoretical approach, the top of the Fe 3*d* occupied valence band is set at 0 eV. Note that in our comparison with the experimental results in Figs. 4(b) and 4(c), this peak was shifted by 1.5 eV to match the experimental results. Both GGA and GGA+*U* methods give similar density of states in the O 2*p* region, with the sharp Si 3*s* feature (band 5) at similar energies (about 10 eV). The overall dispersion of the entire valence band of about 10 eV for the GGA calculation is in good agreement with the experimental dispersion [Fig. 4(b)]. In contrast, the GGA+*U* calculation yields a more condensed valence band of about 8 eV. As might be expected, however, the GGA calculation gives suspect results in the low-energy Fe 3*d* region and much poorer agreement with experiment in the low-energy region. For example, the GGA calculation gives *three* distinct bands at low BE, compared to the *two* distinct bands for the GGA+*U* calculations on both the Mg-rich olivine and fayalite, which have been formally assigned to the Fe 3*d* t_{2g} and e_g orbitals by us and in previous theoretical studies.[26,37] The three distinct Fe 3*d* bands in the GGA calculation are surprising. Moreover, the GGA calculation seriously underestimated the band gap. However, a band gap of about 3 eV is correctly predicted by the GGA+*U* calculation.

The differences in the two calculations become more apparent using the Fe density of states by spin type [Fig. 10(a)] and using the total number of Fe 3*d* density electrons as a function of the binding energy [Fig. 10(b)]. Again, the energy scales are set by fixing the top of the valence band at 0 eV. The Fe in these olivines is present as high-spin Fe^{2+} with six 3*d* electrons, five spin up and one spin down. The spin-down electron at 0 eV [Figs. 10(a) and 10(b)] gives rise in both cases to band 1 in the spectra at 1.5 eV in Fig. 4(b).

About two of the spin-up electrons in both calculations (at 1.4 eV for GGA+U and 2.0 eV for the GGA calculation) give rise to band 2 at about 2.9 eV. The sharp band in the GGA calculation at about 3 eV (not seen in the experimental spectrum) is spread out in the GGA+U calculation and loses its distinct features [Fig. 10(b)]. Thus the GGA+U calculation indicates a smaller Fe-O covalent interaction than in the GGA calculation. Although the GGA calculations give better agreement with the overall dispersion of the filled bands in Fe-doped forsterite, GGA+U calculations are required to reproduce the band gap.

V. CONCLUSIONS

High-resolution valence-band XPS spectra have been obtained for quartz and, for the first time, two olivines in the forsterite-fayalite series $(Mg,Fe)_2SiO_4$. Total linewidths of about 1.3 eV are observed for several peaks in the core-level and valence-band spectra. These linewidths are much narrower than previously observed for the core-level and VBXPS spectra of nonconductor silicates. The quartz and olivine valence-band spectra are very different, with the Si $3p-$O $2p$ region of the olivine spectra being both simpler and energetically more condensed than the Si $3p-$O $2p$ region of the quartz spectrum. High-quality band-structural calculations, using pseudopotential density functional theory, yield theoretical XPS spectra in the Gelius approximation which are in quantitative agreement with the experimental spectrum for quartz and in good qualitative agreement for the olivines. The theoretical partial densities of states enable us to assign with confidence all the features in these valence-band spectra using initial-state arguments. The valence-band spectra are sensitive to the nature of the cation in the second-coordination sphere of tetrahedrally coordinated Si atoms. The second-coordination sphere exerts primary control on the dispersion of silicate valence bands by determining the electron density on the O atoms at the apices of Si tetrahedral, but Si $3s$ splitting due to polymerization also contributes to dispersion. The spectra and calculations indicate that the Mg-O bond in olivine is highly ionic, whereas the Fe-O bond is much more covalent.

ACKNOWLEDGMENTS

This study was funded by the Natural Science and Engineering Research Council (NSERC) of Canada. We would like to thank Surface Science Western for all their technical help with the Kratos XPS and the South Australian Museum (Dr. Allan Pring) for providing the olivine mineral samples.

*Electronic address: herzog@erdw.ethz.ch

[1] O. S. Pokrovsky and J. Schott, Geochim. Cosmochim. Acta **64**, 3299 (2000) and references therein.
[2] J. Schott and R. A. Berner, Geochim. Cosmochim. Acta **47**, 2233 (1983).
[3] H. Seyama and M. Soma, Anal. Sci. **19**, 487 (2003) and references therein.
[4] H. Seyama, M. Soma, and A. Tanaka, Chem. Geol. **129**, 209 (1996).
[5] W. A. Casey, M. Hochella, and H. Westrich, Geochim. Cosmochim. Acta **57**, 785 (1993).
[6] H. W. Nesbitt, A. G. Berlich, S. L. Harmer, I. Uhlig, G. M. Bancroft, and R. Szargan, Am. Mineral. **89**, 382 (2004) and references therein.
[7] V. Eyert, K. H. Hock, S. Fiechter, and H. Tributsch, Phys. Rev. B **57**, 6350 (1998) and references therein.
[8] B. Fischer, R. A. Pollak, T. H. DiStefano, and W. D. Grobman, Phys. Rev. B **15**, 3193 (1977).
[9] A. Di Pomponio, A. Continenza, L. Lozzi, M. Passacantando, S. Santucci, and P. Picozzi, Solid State Commun. **95**, 313 (1995).
[10] M. A. Al-Kadier, C. Tolon, and D. S. Urch, J. Chem. Soc., Perkin Trans. 2 **80**, 669 (1984).
[11] D. S. Urch, Miner. Mag. **53**, 153 (1989).
[12] W. Y. Ching, R. A. Murray, D. J. Lam, and B. W. Veal, Phys. Rev. B **28**, 4724 (1983).
[13] N. Jiang, J. D. Denlinger, and J. C. H. Spence, J. Phys.: Condens. Matter **15**, 5523 (2003).
[14] A. M. Asunskis, K. J. Gaskell, D. J. Asunskis, and P. M. A. Sherwood, J. Vac. Sci. Technol. A **21**, 1126 (2003), and references.
[15] T. H. DiStefano and D. E. Eastman, Phys. Rev. Lett. **27**, 1560 (1971).
[16] J. R. Chelikowsky and M. Schluter, Phys. Rev. B **15**, 4020 (1977).
[17] R. Dovesi, C. Pisani, C. Roetti, and B. Silvi, J. Chem. Phys. **86**, 6967 (1987).
[18] J. A. Tossell and D. J. Vaughan, *Theoretical Geochemistry: Mechanics in the Earth and Mineral Sciences* (Oxford University Press, New York, 1992), pp. 172–175 and references therein.
[19] L. A. J. Garvie, P. Rez, J. R. Alvarez, P. R. Busek, A. J. Craven, and R. Brydson, Am. Mineral. **85**, 732 (2000), and references therein.
[20] J. A. Tossell, Am. Mineral. **62**, 136 (1977).
[21] J. A. Tossell and D. J. Vaughan, *Theoretical Geochemistry: Mechanics in the Earth and Mineral Sciences* (Oxford University Press, New York, 1992), pp. 217–227 and references therein.
[22] T. L. Barr, *Modern ESCA, The Principles ands Practice of X-ray Photoelectron Spectroscopy* (CRC Press, Baca Raton, FL, 1993).
[23] J. Cazaux, J. Electron Spectrosc. Relat. Phenom. **105**, 155 (1999).
[24] Kratos web page: http://www.kratos.com
[25] H. W. Nesbitt, G. M. Bancroft, R. Davidson, N. S. McIntyre, and A. R. Pratt, Am. Mineral. **89**, 878 (2004).
[26] B. Silvi, A. Bouaziz, and Ph. D'Arco, Phys. Chem. Miner. **20**, 333 (1993).
[27] M. Kitaura, H. Nakagawa, and A. Ohnishi, J. Phys. Soc. Jpn. **71**, 2736 (2002).
[28] M. Cococcioni, A. Dal Corso, and S. de Gironcoli, Phys. Rev. B **67**, 094106 (2003).
[29] D. G. J. Sutherland, M. Kasrai, G. M. Bancroft, Z. F. Liu, and K.

H. Tan, Phys. Rev. B **48**, 14989 (1993).
[30] *X-ray Data Booklet*, edited by A. C. Thompson and D. Vaughan (Lawrence Berkeley Laboratory, Berkeley, 2001).
[31] D. A. Shirley, Phys. Rev. B **5**, 4709 (1972).
[32] J. P. Perdew, K. Burke, and M. Ernzerhof, Phys. Rev. Lett. **77**, 3865 (1996).
[33] P. Ordejón, E. Artacho, and J. M. Soler, Phys. Rev. B **53**, R10441 (1996); J. M. Soler, E. Artacho, J. D. Gale, A. García, J. Junquera, P. Ordejón, and D. Sánchez-Portal, J. Phys.: Condens. Matter **14**, 2745 (2002).
[34] N. Troullier and J. L. Martins, Phys. Rev. B **43**, 1993 (1991).
[35] O. F. Sankey and D. J. Niklewski, Phys. Rev. B **40**, 3979 (1989).
[36] R. W. G. Wyckoff, *Crystal Structures*, 2nd ed. (Krieger, Malabar, FL, 1981), Vol. 3.
[37] V. I. Anisimov, F. Aryasetiawan, and A. I. Liechtenstein, J. Phys.: Condens. Matter **9**, 767 (1997).
[38] G. Kresse and J. Furthmüller, Comput. Mater. Sci. **6**, 15 (1996); Phys. Rev. B **54**, 11169 (1996).
[39] X. Jiang and G. Y. Guo, Phys. Rev. B **69**, 155108 (2004).
[40] U. Gelius, in *Electron Spectroscopy*, edited by D. A. Shirley (North-Holland, Amsterdam, 1972), pp. 311–34.
[41] J. J. Yeh and I. Lindau, At. Data Nucl. Data Tables **32**, 1 (1985).
[42] M. Kyono, M. Kimata, and T. Hatta, Naturwiss. **90**, 2003 (2003).
[43] H. Seyama, D. Wang, and M. Soma, Surf. Interface Anal. **36**, 609 (2004).
[44] F. J. Himpsel, F. R. McFeely, A. Taleb-Ibrahimi, J. A. Yarmoff, and G. Hollinger, Phys. Rev. B **38**, 6084 (1988).
[45] J. A. Leiro, K. Laajalehto, I. Kartio, and M. H. Heinonen, Surf. Sci. **412**, L918 (1998).
[46] B. W. Yates, K. H. Tan, G. M. Bancroft, L. L. Coatsworth, and J. S. Tse, J. Chem. Phys. **83**, 4906 (1985).
[47] R. G. Burns, *Mineralogical Applications of Crystal Field Theory*, 2nd ed. (Cambridge University Press, Cambridge, England, 1993), pp. 161–164, and references therein.
[48] W. Gonschorek, Process Control Qual. **13**, 337 (1986).
[49] P. W. Langhoff, S. R. Langhoff, T. N. Rescigno, J. Scgirmer, L. S. Cederbaum, W. Domke, and W. Von Neissen, Chem. Phys. **58**, 71 (1981), and references therein.
[50] W. Temesghen and P. M. A. Sherwood, Anal. Bioanal. Chem. **373**, 601 (2002) and references therein.
[51] C.-Y. Kim, M. J. Bedzyk, E. J. Nelson, J. C. Woicik, and L. E. Berman, Phys. Rev. B **66**, 085115 (2002).
[52] R. J. Lad and V. E. Henrich, Phys. Rev. B **39**, 13478 (1989).
[53] R. G. Egdell, I. L. Fragala, and A. F. Orchard, J. Electron Spectrosc. Relat. Phenom. **17**, 267 (1979).
[54] M. P. Keane, A. NavesdeBrito, N. Correia, S. Svensson, L. Karlsson, B. Wannberg, U. Gelius, S. Lunell, W. R. Salaneck, M. Logdlund, D. B. Swanson, and A. G. MacDiarmid, Phys. Rev. B **45**, 6390 (1992).
[55] S. Mahl, M. Neumann, B. Schneider, V. Schlett, and A. Baalmann, J. Polym. Sci., Part A: Polym. Chem. **37**, 95 (1999) and references therein.